PHYSICAL REVIEW A **77**, 032336 (2008)

Spontaneous parametric down-conversion: Anisotropical and anomalously strong narrowing of biphoton momentum correlation distributions

M. V. Fedorov, M. A. Efremov, and P. A. Volkov
A. M. Prokhorov General Physics Institute of Russian Academy of Sciences, 117942, Moscow, Russia

E. V. Moreva*
Moscow Engineering Physics Institute (State University), 115409, Moscow, Russia

S. S. Straupe and S. P. Kulik
Faculty of Physics, Moscow State University, 119992, Moscow, Russia

(Received 27 July 2007; published 24 March 2008)

We show that the wave packet of a biphoton generated via spontaneous parametric down-conversion is strongly anisotropic. Its anisotropic features manifest themselves very clearly in comparison with measurements performed in two different schemes: When the detector scanning plane is perpendicular or parallel to the plane containing the crystal optical axis and the laser axis. The first of these two schemes is traditional whereas the second one gives rise to such unexpected results, such as anomalously strong narrowing of the biphoton wave packet measured in the coincidence scheme and very high degree of entanglement. The results are predicted theoretically and confirmed experimentally.

DOI: 10.1103/PhysRevA.77.032336 PACS number(s): 03.67.Mn, 42.65.Lm, 03.65.Ud

I. INTRODUCTION

Quantum entanglement is one of the surprising consequences of quantum mechanics. It is in the center of attention since the famous paper by Einstein, Podolsky, and Rosen [1] (EPR). Two (or more) subsystems are entangled if the system as a whole is characterized by a wave function or a density matrix, which cannot be presented in the form of products of subsystems' wave functions or density matrices [2]. Entanglement is the key element of such phenomena and domains of modern quantum optics, such as quantum teleportation, quantum cryptography, Bell violation experiments, and quantum computation.

A special class of entangled systems, attracting a permanently growing attention, is that of systems with continuous variables. The most often and widely studied example is spontaneous parametric down-conversion (SPDC) [3–13]. However, there are many other processes of decaying bipartite systems characterized by continuous variables, for which the concept of entanglement is applicable and investigation of the corresponding problems is interesting enough. Some examples considered earlier are photoionzation of atoms and photodissociation of molecules [14], spontaneous emission of a photon by an atom [15], and multiphoton production of electron-positron pairs [16].

In this paper we concentrate our attention on SPDC, and the subject of investigation consists in describing theoretically and observing experimentally photon angular distributions in near and far zones. Compared to earlier investigations, we take into account more carefully anisotropy of the refractive index in a nonlinear crystal. We show that this can give rise to a strong anisotropy of coincidence angular distributions. In the geometry of measurements (to be specified below), where the anisotropy is most strongly pronounced, the coincidence angular distribution in a far zone will be shown to be much narrower than both the same distribution in the orthogonal geometry and the pump. Such an anisotropic and very strong narrowing of the coincidence distributions is related to a very high degree of entanglement that can be accumulated in SPDC biphoton states.

Note that in Ref. [17] a strong anisotropy was found to occur in the coincidence biphoton spatial (coordinate) distributions. The SPDC configuration considered in Ref. [17] corresponded to the regime of noncollinear parametric scattering, and the biphoton spatial distributions were investigated in the near zone, i.e., just at the crystal exit surface. In contrast, we consider here the collinear SPDC configuration and we investigate the angular biphoton distributions in the far zone. Relation between the coordinate and angular distributions in this configuration is an interesting problem to which we hope to return elsewhere.

II. PARAMETERS CHARACTERIZING THE DEGREE OF ENTANGLEMENT

A. Schmidt number

For pure bipartite states, one of the most appropriate parameters to quantify the degree of entanglement is the Schmidt number K [18,19]. In a general form its definition is rather simple and straightforward. If a system under consideration is characterized by a wave function $\Psi(1,2)$ with variables 1 and 2, the corresponding density matrix is given by $\rho=\Psi\Psi^{\dagger}$. By taking the trace with respect to, e.g., the second particle variable 2, one gets the reduced density matrix $\rho_r=\mathrm{Tr}_2(\rho)$. In terms of ρ_r, the Schmidt number is defined as

$$K=[\mathrm{Tr}_1(\rho_r^2)]^{-1}. \tag{1}$$

In the case of continuous variables traces turn into integrals. Qualitatively, the Schmidt number K determines the minimal

---

*ekaterina.moreva@gmail.com

number of products of single-particle functions for which the original bipartite function $\Psi(1,2)$ can be expanded. The inverse value of K, K^{-1}, is known as purity, and it shows how much the reduced single-particle state (characterized by ρ_r) differs from a pure one. In the case of nonentangled states, i.e., when the bipartite wave function factorizes, $\Psi(1,2)=\psi_1(1)\psi_2(2)$, the Schmidt number is equal to 1, $K=1$. In other cases $K>1$, and the larger values of K indicate a higher degree of entanglement. Unfortunately, the described definition of the Schmidt number does not show how this parameter could be measured experimentally. Moreover, sometimes, for complicated entangled wave functions with two-dimensional (2D) or three-dimensional (3D) continuous variables, even calculations of the Schmidt number can be difficult. For these reasons alternative quantifiers of the degree of entanglement are needed.

B. Wave-packet width-ratio parameters

One of such alternative approaches to the entanglement characterization is based on the analysis of conditional and unconditional probability density distributions, which are related directly to experimentally measurable coincidence and single-particle wave packets of particles. Specifically, in the works [13–15] it was suggested to characterize the degree of entanglement by the width-ratio parameters

$$R_x=\frac{\Delta x_{1,2}^{(s)}}{\Delta x_{1,2}^{(c)}} \quad \text{or} \quad R_k=\frac{\Delta k_{1,2}^{(s)}}{\Delta k_{1,2}^{(c)}}, \tag{2}$$

where Δx and Δk are the coordinate or momentum wave-packet widths, superscripts (s) and (c) refer to single-particle and coincidence measurements, and subscripts (1,2) refer to particles 1 and 2. The single-particle and coincidence wave-packet widths entering Eqs. (2) can be either measured experimentally or calculated with the help of, correspondingly, unconditional and conditional single-particle probability distributions:

$$\frac{dw^{\text{uncond}}}{dx_1}=\int dx_2|\Psi(x_1,x_2)|^2,$$

$$\frac{dw^{\text{cond}}}{dx_1}=\left.\frac{|\Psi(x_1,x_2)|^2}{\displaystyle\int dx_1|\Psi(x_1,x_2)|^2}\right|_{\text{at a given } x_2}. \tag{3}$$

Expressions similar to those of Eqs. (3) connect the momentum-representation probability distributions with the momentum wave function $\tilde{\Psi}(k_1,k_2)$. The latter is a double-Fourier transform of $\Psi(x_1,x_2)$, with respect to the variables x_1 and x_2. In units with $\hbar=1$ we do not make any distinction between momenta and wave vectors of photons or any other particles.

In the case of nonentangled (factorized) states, $\Psi(x_1,x_2)=\psi_1(x_1)\psi_2(x_2)$, the conditional and unconditional probability distributions of Eq. (3) identically coincide with each other, $dw^{\text{cond}}/dx_1\equiv dw^{\text{uncond}}/dx_1=|\psi_1(x_1)|^2$, as well as their widths, $\Delta x_1^{(c)}=\Delta x_1^{(s)}$. Hence, in nonentangled states $R=1$. Any deviations from exact coincidence of the conditional and unconditional probability distributions is an indication that the bipartite state under consideration is entangled. The width-ratio parameter R is the simplest, and easily measurable experimentally, macroscopic characteristic of a difference between the conditional and unconditional probability distributions and, hence, it can be considered as a quantifier of the degree of entanglement. Similarly to the Schmidt number, the width-ratio parameter R is larger than one in the case of entangled states, $R>1$, and the larger values of R indicate a higher degree of entanglement.

As it was shown in Ref. [13], the parameters R_x, R_k, and K coincide with each other for a rather general class of double-Gaussian bipartite wave functions

$$\Psi_{\text{DG}}(x_1,x_2)\propto\exp\left(-\frac{(\alpha x_1+\beta x_2)^2}{2a^2}\right)\exp\left(-\frac{(\gamma x_1+\delta x_2)^2}{2b^2}\right), \tag{4}$$

where the constants α, β, γ, δ and a, b are different for different problems and are determined by the physics of these problems. For the wave function of Eq. (4) the explicit expressions for $R_x=R_k=K$ was found to be given by [13]

$$R_x=R_k=K=\frac{\sqrt{\alpha^2b^2+\gamma^2a^2}\sqrt{\beta^2b^2+\delta^2a^2}}{ab|\alpha\delta-\beta\gamma|}. \tag{5}$$

This theorem and the possibility of measuring R parameters (2) experimentally open a way of measuring the degree of entanglement. Also, the identity of R and K for the double-Gaussian wave functions confirms that interpretation of the width-ratio parameter R as the entanglement quantifier is quite reasonable. It is important also that the width-ratio parameters R do not depend on how specifically the wave-packet widths are defined (in contrast to other entanglement parameters discussed below).

Note however that, in principle, the width-ratio parameter R can take different values (a) in the momentum and coordinate representations (owing to spreading of coordinate wave packets for massive particles [14]) and (b) in differing geometries of measurements for anisotropic 2D or 3D states (to be shown in this paper). In all such cases this is the largest measurable value of the width-ratio parameter that characterizes appropriately the degree of entanglement.

Finally, sometimes double-Gaussian bipartite wave functions of the form of that given by Eq. (4) arise rather naturally. One example is the multiphoton electron-positron pair production where the electron-positron bipartite wave function is determined by the Gaussian shape of the pulse envelopes of two electromagnetic waves producing pairs [16]. In other cases the arising bipartite wave functions are non-Gaussian but they are simple enough to be successfully modeled by double-Gaussian wave functions [14,15]. However, sometimes bipartite wave functions appear to be much more complicated, which makes their direct modeling by the double-Gaussian wave functions impossible. An example of such a situation is just the SPDC process considered in this paper.

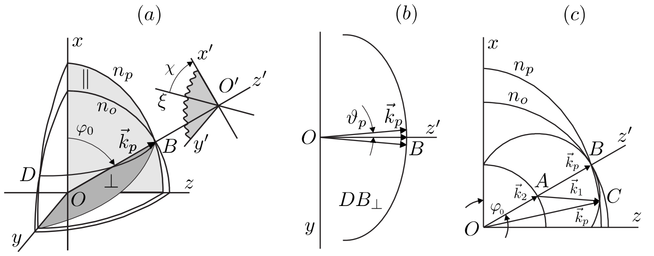

FIG. 1. (a) Octant of the refractive index surfaces $n_e(\vec{r})$ and $n_o(\vec{r})$ for pump and emitted photons, (b) and (c) are two perpendicular sections by the planes ⊥ and ∥ shaded in (a); $DB_\perp$ is the projection on the ⊥ plane of the sphere-ellipsoid crossing circle shown partially by the arc DB in (a); ϑ_p is the angle between $\vec{k}_p$ and the z' axis; φ_0 is the angle between the crystal optical axis and the laser axis; χ is the angle between the observation direction $O'\xi$ and the $O'x'$ axis.

C. EPR entanglement parameter

Finally, the degree of entanglement of bipartite systems can be characterized by the EPR parameter defined as the inverse product of the conditional coordinate and momentum uncertainties or wave-packet widths

$$C_{\rm EPR}=\frac{1}{\Delta x_1^{(c)}\Delta k_1^{(c)}}. \tag{6}$$

For singular δ-function states considered in the paper by Einstein, Podolsky, and Rosen [1] the conditional uncertainty product equals zero and $C_{\rm EPR}=\infty$. For double-Gaussian wave functions of the form (4) with the appropriately defined wave-packet widths, the EPR parameter was shown [13,15] to coincide identically with the Schmidt number, $C_{\rm EPR}=K$. In the limit of nonentangled states $C_{\rm EPR}=1$. Specifically for SPDC, the EPR uncertainty product was measured experimentally [12] and was found to be finite and less than 1.

In this work we do not calculate or measure either the EPR parameter or Schmidt number. We concentrate our attention on the analysis of the coincidence and single-particle wave-packet structures and the width-ratio parameter R. Anisotropy effects are appropriately taken into account and are shown to play a crucial role both for characterization of the wave-packet form and for production of biphoton states with very high degree of entanglement.

III. THEORETICAL DESCRIPTION

A. Derivation of the main general expressions

Let us consider a collinear and degenerate type-I SPDC process, when an extraordinary pump photon of a frequency ω_p decays in two ordinary photons $e\to o+o$ with equal frequencies $\omega_p/2$ and propagating more or less along the pump beam. In 3D, refractive index surfaces for extraordinary $[n_e(\vec{r};\omega_p)]$ and ordinary $[n_o(\vec{r};\omega_p/2)]$ waves in an anisotropic crystal are, correspondingly, an ellipsoid and a sphere. Figure 1(a) shows one octant of these figures and its sections by three coordinate planes (xz), (xy), and (yz). In this picture, the optical axis (OA) of a crystal is taken directed along the Ox axis, and the orthogonal axes Oy and Oz are chosen in such a way that the (xz) plane contains the pump laser axis (LA), Oz'. The arc DB in Fig. 1(a) is a part of the circle by which the sphere and ellipsoid cross each other. We assume that LA is directed strictly to the point B where the arc DB crosses the xz plane. This means that the pump and emitted photons propagating strictly along the z' axis obey the collinear degenerate phase-matching condition: $k_1=k_2=k_p/2$ at $\vec{k}_p\|\vec{k}_1\|\vec{k}_2\|Oz'$. This assumption predetermines a value of the angle φ_0 between OA and LA. For LiIO$_3$ crystal and the pump wavelength $\lambda_p=325$ nm (as in the experiment described in Sec. IV) this angle appears to be equal to $\varphi_0=60.44°$.

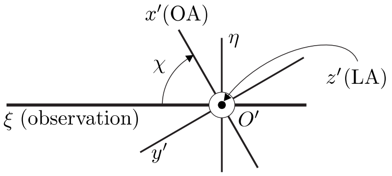

FIG. 2. Geometry of the experiment: The laser axis Oz' is directed horizontally and straight toward the observer; the detector installation line $O'\xi$ is horizontal; the plane containing the crystal optical axis and varying its orientation is $(x'z')$; χ is a varying angle determining the crystal orientation.

In our consideration we assume that the pump is not a single plane wave but is given by a coherent superposition of plane waves with wave vectors $\vec{k}_p$ filling in a cone, the axis of which coincides with LA Oz', and the pump angular width α is finite.

O' in Fig. 1(a) is some point in a far zone located at LA Oz' and such that detectors registering photons are located in the plane perpendicular to Oz' and containing the point O'. The axes $O'x'$ and $O'y'$ in this plane are perpendicular to each other and to $O'z'$, and $O'x'\in(xz)$, $O'y'\|Oy$. This means, in particular, that the plane $(x'z')$ contains OA.

In Fig. 1(a) the position of OA is taken constant (OA$\|Oz$), we can assume that detectors are installed along some line $O'\xi$, orientation of which in the plane $(x'y')$ can be varied. Under this assumption, detectors register only photons (1) or (1) and (2) with wave vectors $\vec{k}_1$ and $\vec{k}_2$ belonging to the plane $(z'\xi)$. Two limiting positions of the observation direction Ox' correspond to $O'\xi=O'y'\|Oy$ and $O'\xi=O'x'\in(xz)$. In these two limiting cases the detectors register only photons with wave vector $\vec{k}_1$ and $\vec{k}_2$ belonging, correspondingly, to the yOz' and xOz planes. In Fig. 1(a) these planes are shaded and they are labeled with the symbols ⊥ and ∥, respectively. Here "perpendicular" and "parallel" mean that the observation plane (i.e., the plane containing wave vectors of photons to be observed) is perpendicular or parallel to the OA-LA plane. Below these two cases are referred to as those of the perpendicular and parallel geometry. Sections of the 3D refractive index surfaces by the ⊥ and ∥ planes are shown in (b) and (c) of Fig. 1.

Note, however, that the idea of changing orientation of the detector-installation line is used here for simplification of illustrations, such as those given in Fig. 1. In real experiment, as shown in Fig. 2, the laser pump axis Oz' was horizontal, as well as the detector installation direction $O'\xi$ and the observation plane $(\xi z')$. Instead of changing the detector installation direction in experiment the crystal itself and its optical axis were rotated around the laser axis. In Fig. 2 the plane containing the crystal optical axis is $(x'z')$. As well as in Fig. 1(a), the angle χ in Fig. 2 is the angle between the $O'x'$ and $O'\xi$ axes, i.e., the angle determining orientation of the OA-LA plane with respect to the observation plane. The cases $O'x' \perp O'\xi$ and $O'x' \parallel O'\xi$ correspond to the above-described $\perp$ and $\parallel$ geometries.

In our further consideration we will use the approximation of a wide crystal in which the momentum conservation rule or the phase-matching condition is satisfied exactly for transverse components of the pump and emitted photon wave vectors

$$\vec{k}_{p\perp} = \vec{k}_{1\perp} + \vec{k}_{2\perp}, \tag{7}$$

where used as a subscript to wave-vector notations, the symbol $\perp$ means perpendicular to the LA, $\perp$ to Oz'. As, by the assumption, the observation plane is $(\xi z')$, the wave vectors of photons to be registered must have the zero η components. In the case of coincidence measurements, both photons (1) and (2) are observed and, hence $k_{1\eta}=k_{2\eta}=k_{p\eta}=0$. On the other hand, in the case of single-particle measurements, the detector registers only one kind of photon [e.g., photons of the type (1)], and this puts only one restriction $k_{1\eta}=0$, whereas both $k_{2\eta}$ and $k_{p\eta}=-k_{2\eta}$ can be different from zero. As we will see below, just such processes with $k_{p\eta}$, $k_{2\eta}\neq 0$ are most important for describing single-particle momentum (angular) distributions of biphotons.

In the wide-crystal approximation we can use the following known [5] and absolutely correct general expression for the biphoton wave function depending on the transverse components of the emitted photon momenta $\vec{k}_{1\perp}$ and $\vec{k}_{2\perp}$,

$$\Psi(\vec{k}_{1\perp},\vec{k}_{2\perp}) \propto E_p^*(\vec{k}_{1\perp}+\vec{k}_{2\perp})\mathrm{sinc}\left(\frac{L\Delta_{z'}}{2}\right), \tag{8}$$

where $E_p(\vec{k}_{p\perp})$ is the Fourier transform of the pump transverse profile amplitude, $\mathrm{sinc}(u)=\sin(u)/u$, L is the crystal length in the z' direction, and $\Delta_{z'}$ is the longitudinal detuning

$$\Delta_{z'} = k_{pz'} - k_{1z'} - k_{2z'} = \sqrt{k_p^2 - k_{p\perp}^2} - \sqrt{k_1^2 - k_{1\perp}^2} - \sqrt{k_2^2 - k_{2\perp}^2}. \tag{9}$$

To simplify further Eq. (9) for the longitudinal detuning, we can use the near-axis approximation in which $|k_{1,2\perp}| \ll k_{1,2}$, $k_{p\perp} \ll k_p$. By expanding square roots in Eq. (9) in powers of transverse components of all the wave vectors and keeping only two first orders we obtain

$$\Delta_{z'} = k_p - k_1 - k_2 + \frac{(\vec{k}_{1\perp}-\vec{k}_{2\perp})^2}{2k_p}. \tag{10}$$

The first term on the right-hand side of Eq. (10) is the detuning from the exact collinear phase-matching condition, $\delta \equiv k_p - k_1 - k_2$. If δ can be taken to be equal zero identically, Eqs. (8) and (10) give immediately the widely known formula [6] (see also [10,13])

$$\Psi(\vec{k}_{1\perp},\vec{k}_{2\perp}) \propto E_p^*(\vec{k}_{1\perp}+\vec{k}_{2\perp})\mathrm{sinc}\left(\frac{L(\vec{k}_{1\perp}-\vec{k}_{2\perp})^2}{4k_p}\right). \tag{11}$$

This formula describes isotropic photon distributions with respect to orientation of wave vectors $\vec{k}_{1\perp}$ and $\vec{k}_{2\perp}$. Though maybe sometimes justified, in a general case this assumption cannot be valid because of an anisotropic nature of a nonlinear crystal itself. As we show below, in the case we consider here anisotropy of a crystal affects very strongly photon angular distributions and makes them strongly anisotropic. Evidently, Eq. (11) is insufficient for describing such an effect and its generalization is needed. Actually, this generalization is provided by the first, generally nonzero, term on the right-hand side of Eq. (10). Let us evaluate the detuning δ more carefully rather than simply setting $\delta=0$.

By the definition, we have $k_p = n_p\omega/c$, where the refractive index n_p depends on the direction of the pump wave vector $\vec{k}_p$. Both direction of the vector $\vec{k}_p$ and its absolute value are completely determined by its transverse ($\perp$ to the laser axis Oz') component $\vec{k}_{p\perp} \equiv \vec{k}_{1\perp}+\vec{k}_{2\perp}$, $k_p = k_p(\vec{k}_{p\perp})$, and $n_p = n_p(\vec{k}_{p\perp})$. In the near axis approximation ($|\vec{k}_{p\perp}| \ll k_p$), the function $n_p(\vec{k}_{p\perp})$ can be approximated by the zero and first orders of its expansion in powers of $\vec{k}_{p\perp}$,

$$n_p(\vec{k}_{p\perp}) = n_o + \left.\vec{k}_{p\perp}\cdot\frac{\partial n_p}{\partial \vec{k}_{p\perp}}\right|_{\vec{k}_{p\perp}=0}, \tag{12}$$

where, owing to the assumption about exact phase matching strictly on the laser axis, $n_o \equiv n_p(\vec{k}_{p\perp}=0)$. Now the collinear phase-matching detuning δ takes the form $\delta = (\omega/c)(\vec{k}_{p\perp}\cdot\partial n_p/\partial\vec{k}_{p\perp})$ and, evidently, this does not equal zero identically.

With Eqs. (7), (8), (10), and (12) combined together, we obtain the following main formula generalizing that of Eq. (11):

$$\Psi(\vec{k}_{1\perp},\vec{k}_{2\perp}) \propto E_p^*(\vec{k}_{1\perp}+\vec{k}_{2\perp})\mathrm{sinc}\left[\frac{L}{2}\left(\frac{\omega}{c}(\vec{k}_{1\perp}+\vec{k}_{2\perp})\cdot\frac{\partial n_p}{\partial\vec{k}_{p\perp}} + \frac{(\vec{k}_{1\perp}-\vec{k}_{2\perp})^2}{2k_p}\right)\right], \tag{13}$$

where, as previously, k_p and $\partial n_p/\partial\vec{k}_{p\perp}$ are taken at $\vec{k}_{p\perp}=0$. The first term in the argument of the sinc function on the right-hand side of Eq. (13) can be slightly simplified if we introduce the unit vector $\vec{e}_g$ in the plane perpendicular to the laser axis directed along the gradient of the function $n_p(\vec{k}_{p\perp})$. Evidently, this unit vector is in the OA-LA plane. Let also ϑ_p be the angle between $\vec{k}_{p\perp}$ and the laser axis in the case when $\vec{k}_{p\perp}$ is in the same OA-LA plane as $\vec{e}_g$. Then $k_{p\perp} = \vartheta_p k_p(0)$, $\partial n_p/\partial\vec{k}_{p\perp} = \vec{e}_g n'_p/k_p(0)$ with $n'_p = dn_p/d\vartheta_p$, and this reduces Eq. (13) to the form

$$\Psi(\vec{k}_{1\perp},\vec{k}_{2\perp}) \propto E_p^*(\vec{k}_{1\perp}+\vec{k}_{2\perp})\,\mathrm{sinc}\left[\frac{L}{2}\left(\frac{n_p'}{n_o}(\vec{k}_{1\perp}+\vec{k}_{2\perp})\cdot\vec{e}_g + \frac{(\vec{k}_{1\perp}-\vec{k}_{2\perp})^2}{2k_p}\right)\right], \tag{14}$$

For LiIO$_3$ crystal and the above-mentioned value of the pump wavelength $\lambda_p=325$ nm, the derivative of the refractive index was found to be $n_p'=-0.1436$, and this value is used in all further estimates.

Finally, in terms of the geometry of Fig. 2, the unit vector $\vec{e}_g$ is directed along the $O'x'$ axis and its projection on the axes $O'\xi$ and $O'\eta$ are equal to cos χ and sin χ, which results in the following expression for the biphoton wave function:

$$\Psi(\vec{k}_{1\perp},\vec{k}_{2\perp}) \propto E_p^*(\vec{k}_{1\perp}+\vec{k}_{2\perp})\,\mathrm{sinc}\left[\frac{L}{2}\left(\frac{n_p'}{n_o}[(k_{1\xi}+k_{2\xi})\cos\chi + (k_{1\eta}+k_{2\eta})\sin\chi] + \frac{(\vec{k}_{1\perp}-\vec{k}_{2\perp})^2}{2k_p}\right)\right]. \tag{15}$$

As we have assumed that wave vectors of all photons to be registered are located in the $z'\xi$ plane, such vectors have zero η projections. In the case of coincidence measurements this condition is valid for both $\vec{k}_1$ and $\vec{k}_2$ vectors. Hence, for calculating the coincidence photon distributions we can use a formula simpler than that of Eq. (15) and given by

$$\Psi^{(c)}(\vec{k}_{1\perp},\vec{k}_{2\perp}) \propto E_p^*(k_{1\xi}+k_{2\xi})\,\mathrm{sinc}\left[\frac{L}{2}\left(\frac{n_p'}{n_o}(k_{1\xi}+k_{2\xi})\cos\chi + \frac{(k_{1\xi}-k_{2\xi})^2}{2k_p}\right)\right], \tag{16}$$

where the superscript (c) means that this expression can be used only for calculating coincidence distributions. In the case of single-photon distributions only photons of one kind are registered, and the η projection of only one wave vector (e.g., $k_{1\eta}$) turns zero, whereas for the other photon the η projection of the wave vector can take nonzero values, $k_{1\eta}\neq 0$. The single-particle distributions are given by the squared wave function of Eq. (15) integrated over $k_{2\xi}$ and $k_{2\eta}$.

Note that in all cases the SPDC emission occurs in small vicinities of the exact phase-matching directions, at which $\vec{k}_1+\vec{k}_2=\vec{k}_p$. If both wave vectors $\vec{k}_1$ and $\vec{k}_2$ are in the observation plane (i.e., if $k_{1\eta}=k_{2\eta}=0$), the exact phase-matching direction coincides with the laser axis and is fulfilled at $\vec{k}_1\parallel\vec{k}_2\parallel Oz'$, and this is the case of collinear phase matching. If, however, $k_{1\eta}=0$ but $k_{2\eta}\neq 0$, the exact phase-matching condition cannot be fulfilled at wave vectors $\vec{k}_p$, $\vec{k}_1$, and $\vec{k}_2$ parallel to each other and to the laser axis Oz'. The exact phase matching occurs, e.g., at $k_{p\xi}=0$, $k_{2\xi}=-k_{1\xi}$, $k_{1\eta}=0$, and $k_{p\eta}=k_{2\eta}$. These are the noncollinear phase-matching conditions. Integration over $k_{2\eta}$, arising in the single-particle distributions, is related to taking into account noncollinear phase-matching SPDC processes.

The assumption that the wave vector $\vec{k}_1$ is located in the observation plane $(z'\xi)$ and $k_{1\eta}=0$ simplifies the general formula of Eq. (15), though not too much. In any case, the dependence of the biphoton wave function Ψ on the angle χ in Eqs. (15) and (16) reflects the anisotropy effects. A difference between the two limiting cases $\chi=0$ and $\chi=\pi/2$ characterizes how strongly the anisotropy of a crystal manifests itself in the coincidence and single-particle photon distributions.

For further comparison with experiment, it is convenient to rewrite the derived general formula [Eq. (15)] in terms of the scattering angles, defined outside the crystal as $\theta_{1,2\xi}=2k_{1,2\xi}/k_p^{(0)}$ and $\theta_{1,2\eta}=2k_{1,2\eta}/k_p^{(0)}$, where $k_p^{(0)}=\omega_p/c$. Below we will set $\theta_{1\eta}=0$ and denote $\theta_{1\xi}\equiv\theta_1$. With these substitutions, Eq. (15) takes the form

$$\Psi(\theta_1,\theta_{2\xi},\theta_{2\eta}) \propto E_p^*\left(\frac{\theta_1+\theta_{2\xi}}{2},\frac{\theta_{2\eta}}{2}\right) \times\mathrm{sinc}\left(\frac{Lk_p^{(0)}}{16n_o}\{4n_p'[(\theta_1+\theta_{2\xi})\times\cos\chi+\theta_{2\eta}\sin\chi] + (\theta_1-\theta_{2\xi})^2+\theta_{2\eta}^2\}\right). \tag{17}$$

In the cases of $\parallel$ and $\perp$ geometries, i.e., correspondingly, at $\chi=0$ and $\chi=\pi/2$, Eq. (17) yields

$$\Psi_{\parallel}(\theta_1,\theta_{2\xi},\theta_{2\eta}) \propto E_p^*\left(\frac{\theta_1+\theta_{2\xi}}{2},\frac{\theta_{2\eta}}{2}\right)\mathrm{sinc}\left(\frac{Lk_p^{(0)}}{16n_o}[4n_p'(\theta_1+\theta_{2\xi}) + (\theta_1-\theta_{2\xi})^2+\theta_{2\eta}^2]\right) \tag{18}$$

and

$$\Psi_{\perp}(\theta_1,\theta_{2\xi},\theta_{2\eta}) \propto E_p^*\left(\frac{\theta_1+\theta_{2\xi}}{2},\frac{\theta_{2\eta}}{2}\right) \times\mathrm{sinc}\left(\frac{Lk_p^{(0)}}{16n_o}[4n_p'\theta_{2\eta}+(\theta_1-\theta_{2\xi})^2+\theta_{2\eta}^2]\right). \tag{19}$$

In accordance with what was mentioned above about the wave vector $\vec{k}_2$, for calculating coincidence distributions we can set in all three last formulas [Eqs. (17)–(19)] $\theta_{2\eta}=0$. By denoting in this case $\theta_{2\xi}=\theta_2$, we obtain

$$\Psi^{(c)}(\theta_1,\theta_2) \propto E_p^*\left(\frac{\theta_1+\theta_2}{2},0\right)\mathrm{sinc}\left(\frac{Lk_p^{(0)}}{16n_o}[4n_p'(\theta_1+\theta_2)\cos\chi + (\theta_1-\theta_2)^2]\right), \tag{20}$$

$$\Psi_{\parallel}^{(c)}(\theta_1,\theta_2) \propto E_p^*\left(\frac{\theta_1+\theta_2}{2},0\right) \times\mathrm{sinc}\left(\frac{Lk_p^{(0)}}{16n_o}[4n_p'(\theta_1+\theta_2)+(\theta_1-\theta_2)^2]\right), \tag{21}$$

and

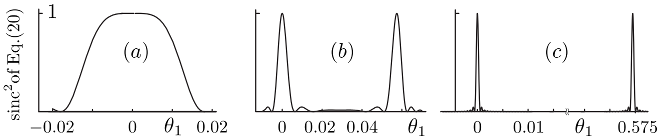

FIG. 3. The sinc^2 function of Eq. (20) at (a) $\chi=90°$, (b) $\chi=84°$, and (c) $\chi=0$, θ_1 in radians.

$$\Psi_{\perp}^{(c)}(\theta_1,\theta_2) \propto E_p^*\left(\frac{\theta_1+\theta_2}{2},0\right)\mathrm{sinc}\left(\frac{Lk_p^{(0)}}{16n_o}(\theta_1-\theta_2)^2\right). \tag{22}$$

Of all the derived equations (13)–(22), only the last one, Eq. (22), corresponds to the wave function of Refs. [6,10,13] given above by Eq. (11). In all other cases the derived expressions differ from those following from Eq. (11) by additional first terms in the arguments of the sinc functions.

B. Anisotropy of the biphoton wave function

The χ-dependent terms in the arguments of sinc functions in Eqs. (15)–(17) and (20) determine the dependence of the biphoton wave function and photon angular distributions on the crystal orientation. To check whether this dependence is well pronounced or not, we plot in Fig. 3 the squared sinc function of Eq. (20) in its dependence on θ_1 at $\theta_2=0$ and three different values of the angle χ. The crystal length is taken equal to $L=1.5$ cm (as in the experiment, Sec. IV).

One can see, that with a decreasing value of the angle χ the structure of the curves in Fig. 3 changes drastically. A single wide peak splits for two peaks, spacing between them grows, and the peaks themselves are getting very narrow. The widths of the only peak at $\chi=90°$ and of narrow peaks at $\chi=0$ are equal to 24 mrad and 0.5 mrad, correspondingly. The ratio of these two widths is equal to 48 and this number characterizes the degree of peak narrowing arising owing to modifications in the formulas of Eqs. (13)–(20) compared to that of Eq. (11).

Mathematically splitting of a single peak for two follows from the quadratic dependence on θ_1 of the function in square brackets on the right-hand side of Eq. (20), at $\theta_2=0$ given by $f(\theta_1)=4n_p'\cos\chi\theta_1+\theta_1^2$. The sinc^2 function is maximal when $f(\theta_1)=0$, and this equation has two different solutions $\theta_1=0$ and $4n_p'\cos\chi$, corresponding to two peaks in the dependence of sinc^2 on θ_1. The only case when these two peaks coincide is $\chi=90°$.

Qualitatively the same conclusions and the same arguments are illustrated by Fig. 1(c). In this figure the vector $\vec{k}_2$ is plotted along the optical axis Oz' ($\theta_2=0$), and it ends at the point A. The ending locus for vectors $\vec{k}_1$ originating from the point A is given in this case by a circle of the radius $n_0/2$ (in units of ω_p/c) and with the center at A. As it is seen from the figure, there are two points B an C where this circle crosses the ellipse $n_p(\theta_p)$ which, in its turn, is the ending locus for the pump wave vectors $\vec{k}_p$. This figure shows that in the case $\chi\neq 90°$ there are two directions of the vectors $\vec{k}_1$ and $\vec{k}_p$ (at a given $\vec{k}_2$) in which the exact phase-matching condition $\vec{k}_p=\vec{k}_1+\vec{k}_2$ appears to be fulfilled. Quantitatively, the nonzero angle of the second exact phase-matching direction appears to be very large. In the case $\chi=0$ the angle $\theta_1=\widehat{BAC}$ in Fig. 1(c) equals approximately 0.57 rad$\approx 32°$ which corresponds to $\theta_p=\frac{1}{2}\theta_1\approx 16°$ for the pump. As the last value is much larger than the pump angular divergence (the maximal pump angular divergence realized in the experiment was $\alpha\sim 4.11$ mrad$\approx 0.24°\ll 16°$), the second (nonzero-angle) peak of the sinc^2 function does not give contributions to the single-particle photon momentum distributions (see the derivation and discussion below). The large-angle second peak of the sinc^2 function was not observed also in the coincidence measurements described in the following section simply because this was out of the detector scanning range. For these reasons we restrict our further analysis by considering only one peak of the sinc^2 function located at small values of the scattering angle θ_1.

Note that if we would take the angle $\theta_2\neq 0$ but, still, given and small ($|\theta_2|\lesssim\alpha$), this would change slightly the positions of the exact phase-matching points B and C in Fig. 1(c). But still they would correspond to strongly different orientation of the pump wave vectors $\overrightarrow{OB}$ and $\overrightarrow{OC}$: a relatively small ($\lesssim\alpha$) angle $\widehat{OB,Oz'}$ and a very large angle $\widehat{OC,Oz'}$. Hence, again, a vicinity of only one exact-phase-matching direction (OB) can be taken into account in the theory and gives its contributions to the experimentally observed photon angular distributions.

On a qualitative level, the peak narrowing, clearly seen in Fig. 3, can be explained also by the quadratic dependence on θ_1 of the sinc^2 argument in Eq. (20), $f(\theta_1)$ at $\theta_2=0$, and by a transition from the case, when the equation $f(\theta_1)=0$ has a single solution (at $\chi=90°$) to the case of two different solutions (at $\chi\neq 90°$). Roughly the peak widths of the sinc^2 function of Eq. (20) can be evaluated from the condition $|f(\theta)|\sim n_o/Lk_p^{(0)}$. In the cases $\chi=90°$ and $\chi=0$ this gives $\Delta\theta_1^{(90°)}\sim 4\sqrt{n_0/Lk_p^{(0)}}$ and $\Delta\theta_1^{(0°)}\sim 4n_0/(Lk_p^{(0)})$. As the product $Lk_p^{(0)}$ is rather large ($\sim 10^5$), both widths are small but the peak widths occurring in the case $\chi=0$ is much narrower than that occurring in the case $\chi=90°$, $n_o/(Lk_p^{(0)})\ll\sqrt{n_o/Lk_p^{(0)}}$.

C. Coincidence distributions

Coincidence distributions of photons are given simply by the squared absolute value of the wave function $\Psi(\theta_1,\theta_2)$ of Eq. (20) at $\theta_2=0$,

$$\frac{dw^{(c)}(\theta_1)}{d\theta_1}\propto|\Psi(\theta_1,0)|^2 \propto\left|E_p^*\left(\frac{\theta_1}{2},0\right)\mathrm{sinc}\left(\frac{Lk_p^{(0)}}{16n_o}(4n_p'\cos\chi\theta_1+\theta_1^2)\right)\right|^2. \tag{23}$$

In accordance with the experimental conditions described below (Sec. IV), the half-height width of the function $|E_p(\theta_p)|^2$ is equal to $\alpha=4.1$ mrad. In dependence on θ_1 this corresponds to a 2-times-larger width of the function $|E_p(\theta_1/2)|^2$, $\Delta\theta_1^{(\mathrm{pump})}=8.2$ mrad. This width is much larger than that of the sinc^2 function at $\chi=0°$ (0.5 mrad) but 3 times smaller than the sinc^2 width at $\chi=90°$ (24 mrad). A general rule is that the coincidence distribution is determined by the narrower of two functions, E_p^2 and sinc^2 in Eq. (23). Hence, for the $\parallel$ ($\chi=0$) and $\perp$ ($\chi=90°$) geometries we obtain

$$\frac{dw_{\parallel}^{(c)}(\theta_1)}{d\theta_1} \propto \mathrm{sinc}^2\left(\frac{Lk_p^{(0)}}{16n_o}(4n'_p\theta_1+\theta_1^2)\right) \approx \mathrm{sinc}^2\left(\frac{Lk_p^{(0)}n'_p}{4n_o}\theta_1\right) \tag{24}$$

and

$$\frac{dw_{\perp}^{(c)}}{d\theta_1} \propto \left|E_p\left(\frac{\theta_1}{2},0\right)\right|^2. \tag{25}$$

D. Single-particle distributions

Single-particle distributions are given by the squared wave function of Eq. (17) integrated over, e.g., $\theta_{2\xi}$ and $\theta_{2\eta}$. In the cases $\chi=0$ and $\chi=90°$ ($\parallel$ and $\perp$ geometries) the wave function of Eq. (17) can be substituted by somewhat simpler ones, (18) and (19). But even in these simpler cases exact calculation of integrals over $\theta_{2\xi}$ and $\theta_{2\eta}$ is hardly possible. Fortunately, there are possibilities of further simplifications and approximate calculations.

In any case for performing integrations we must specify the pump envelope $E_p(\theta_{p\xi},\theta_{p\eta})$. In the experiment of Sec. IV, the most interesting results were obtained with an anisotropic pump. Originally axially symmetric, the pump angular distribution was broadened before entering the crystal with the help of a slit installed along the $O'\eta$ axis. After the slit the pump envelope E_p becomes approximately 3 times wider in its dependence on $\theta_{p\xi}$ than on $\theta_{p\eta}$. In the coordinate representation the dependence of the pump on ξ is given by a superposition of two sgn functions $\frac{1}{4}[\mathrm{sgn}(\xi+d/2)+\mathrm{sgn}(d/2-\xi)]$, where d is the width of the slit and in the experiment we have $d=70\ \mu$m. The dependence of E_p on the angle $\theta_{p\xi}$ is determined by the Fourier transform of this function, which is the sinc function

$$\begin{aligned} E_p(\theta_{p\xi},\theta_{p\eta}) &\propto \mathrm{sinc}\left(\frac{k_p^{(0)}d}{2}\theta_{p\xi}\right)\exp\left(-\frac{2\ln(2)}{\alpha_0^2}\theta_{p\eta}^2\right) \\ &= \mathrm{sinc}\left(\frac{k_p^{(0)}d}{4}(\theta_1+\theta_{2\xi})\right)\exp\left(-\frac{\ln(2)}{2\alpha_0^2}\theta_{2\eta}^2\right). \end{aligned} \tag{26}$$

The numerically found half-height width of the function sinc$^2(u)$, depending on a dimensionless variable u, is equal to $\Delta u=2.784$. This gives for the slit-broadened ($\theta_{p\xi}$-dependent) part of the pump $\Delta\theta_{p\xi}=\alpha=2.784\times(2/k_p^{(0)}d)=4.114$ mrad. However, the slit does not affect the pump angular distribution in the η direction, and we take it to be Gaussian with the width $\Delta\theta_{p\eta}=\alpha_0=1.5$ mrad.

(a) $\parallel$ *geometry.* As on the average, $\theta_{2\eta}^2$ is 7.5 times smaller than $\theta_{2\xi}^2$ and because $\theta_{2\eta}^2/2$ is the only $\theta_{2\eta}$-dependent small positive term in the argument of the sinc function in Eq. (18), approximately this term in this equation can be dropped. With this simplification, integration of the function integration over $\theta_{2\eta}$ contributes only to the normalization factor of the single-particle distribution. In the framework of our consideration this additional normalization factor can be dropped together with all other constant factors we do not specify to give

$$\begin{aligned} \frac{dw_{\parallel}^{(s)}}{d\theta_1} \propto \int d\theta_{2\xi}\,\mathrm{sinc}^2\left(\frac{k_p^{(0)}d}{4}(\theta_1+\theta_{2\xi})\right) \\ \times\mathrm{sinc}^2\left(\frac{Lk_p^{(0)}}{16n_o}[4n'_p(\theta_1+\theta_{2\xi})+(\theta_1-\theta_{2\xi})^2]\right). \end{aligned} \tag{27}$$

Substitution of the integration variable $\theta_{2\xi}\to\theta_{p\xi}=\frac{1}{2}(\theta_{2\xi}+\theta_1)$ reduces Eq. (27) to the form

$$\begin{aligned} \frac{dw_{\parallel}^{(s)}}{d\theta_1} \propto \int d\theta_{p\xi}\,\mathrm{sinc}^2\left(\frac{k_p^{(0)}d}{2}\theta_{p\xi}\right) \\ \times\mathrm{sinc}^2\left(\frac{Lk_p^{(0)}}{4n_o}[2n'_p\theta_{p\xi}+(\theta_{p\xi}-\theta_1)^2]\right). \end{aligned} \tag{28}$$

Similarly to the above-discussed sinc^2 function of Eqs. (21) (at $\theta_2=0$) and (24), the second sinc^2 function in the integrand has two very narrow maxima in dependence on $\theta_{p\xi}$. Positions of these maxima $\theta_{p\xi}^{\pm}$ are determined as solutions of the quadratic equation $2n'_p\theta_{p\xi}+(\theta_{p\xi}-\theta_1)^2=0$, and they are given by

$$\theta_{p\xi}^{\pm}(\theta_1)=(\theta_1-n'_p\mp\sqrt{n_p'^2-2n'_p\theta_1}). \tag{29}$$

Only one of these two solutions is small enough to fall within the pump localization range [the first sinc^2 function in the integrand of Eq. (28)]. As $n'_p<0$, this solution is $\theta_{p\xi}^{+}(\theta_1)$. Near this point the argument of the second sinc^2 function in the integrand of Eq. (28) can be approximated by a linear function

$$\frac{Lk_p^{(0)}}{2n_o}\sqrt{n_p'^2-2n'_p\theta_1}(\theta_{p\xi}-\theta_{p\xi}^{+}), \tag{30}$$

and the sinc^2 function itself can be approximated by the δ function

$$\mathrm{sinc}^2\left(\frac{Lk_p^{(0)}}{4n_o}[2n'_p\theta_{p\xi}+(\theta_{p\xi}-\theta_1)^2]\right) \propto \frac{\delta(\theta_{p\xi}-\theta_{p\xi}^{+})}{\sqrt{n_p'^2-2n'_p\theta_1}}. \tag{31}$$

By substituting this expression into the integrand of Eq. (28), we take the integral and get finally the following simple expression for the single-particle angular distribution of photons in the $\parallel$ geometry:

$$\frac{dw_{\parallel}^{(s)}(\theta_1)}{d\theta_1} \propto \frac{\mathrm{sinc}^2\left(\frac{k_p^{(0)}d}{2}\theta_{p\xi}^{+}(\theta_1)\right)}{\sqrt{n_p'^2-2n'_p\theta_1}} \tag{32}$$

with $\theta_{p\xi}^{+}(\theta_1)$ given by Eq. (29). For analytical estimates it is convenient to simplify slightly Eqs. (29) and (32) by expanding these expression in powers of θ_1 up to the first nonzero terms. The results are given by $\theta_{p\xi}^{+}(\theta_1)\approx\theta_1^2/2|n'_p|$ and

$$\frac{dw_{\parallel}^{(s)}}{d\theta_1} \propto \mathrm{sinc}^2\left(\frac{k_p^{(0)}d}{4|n'_p|}\theta_1^2\right)=\mathrm{sinc}^2\left(\frac{2.784\theta_1^2}{2|n'_p|\alpha}\right). \tag{33}$$

(b) ⊥ *geometry.* In a general form the single-particle photon angular distribution in the ⊥ geometry is given by the squared wave function of Eq. (19) integrated over $\theta_{p\xi} \equiv \frac{1}{2}(\theta_{2\xi}+\theta_1)$ and $\theta_{p\eta} \equiv \frac{1}{2}\theta_{2\eta}$, with the pump E_p^* given by Eq. (26),

$$\frac{dw_\perp^{(s)}(\theta_1)}{d\theta_1} \propto \int d\theta_{p\xi} d\theta_{p\eta} \mathrm{sinc}^2\left(\frac{k_p^{(0)}d}{2}\theta_{p\xi}\right) \times \exp\left(-\frac{4\ln(2)}{\alpha_0^2}\theta_{p\eta}^2\right) \times \mathrm{sinc}^2\left(\frac{Lk_p^{(0)}}{4n_o}[2n_p'\theta_{p\eta}+(\theta_1-\theta_{p\xi})^2+\theta_{p\eta}^2]\right). \tag{34}$$

Again, the last sinc^2 function in the integrand of this equation is characterized by a double-peak curve with very narrow peaks. But now this structure occurs in the dependence of sinc^2 on $\theta_{p\eta}$ [rather than on $\theta_{p\xi}$ as it was in the ∥ geometry, Eq. (28)]. As previously, location of peaks is determined by the condition that the argument of the last sinc^2 function in the integrand of Eq. (34) turns zero. This gives rise to a quadratic equation which has solutions

$$\theta_{p\eta}^{\pm}(\theta_1,\theta_{2\xi}) = -n_p' \mp \sqrt{n_p'^2-(\theta_1-\theta_{2\xi})^2}. \tag{35}$$

Again only one of these two solutions ($\theta_{p\eta}^+$) falls within the pump localization range, and near this point the last sinc^2 function in the integrand of Eq. (34) can be approximated by the δ function $\delta[\theta_{p\eta}-\theta_{p\eta}^+(\theta_1,\theta_{2\xi})]$ to give

$$\frac{dw_\perp^{(s)}(\theta_1)}{d\theta_1} \propto \int d\theta_{p\xi} \mathrm{sinc}^2\left(\frac{k_p^{(0)}d}{2}\theta_{p\xi}\right) \times \exp\left(-\frac{4\ln(2)}{\alpha_0^2}[\theta_{p\eta}^+(\theta_1,\theta_{2\xi})]^2\right) \tag{36}$$

with $\theta_{p\eta}^+(\theta_1,\theta_{2\xi})$ determined by Eq. (35). The remaining integration over $\theta_{2\xi}$ can be performed only numerically. The integration is greatly facilitated if the square root in Eq. (35) is expanded in powers of $\theta_1-\theta_{2\xi}$. As a result, Eq. (36) takes the form

$$\frac{dw_\perp^{(s)}(\theta_1)}{d\theta_1} \propto \int d\theta_{p\xi}\, \mathrm{sinc}^2\left(\frac{k_p^{(0)}d}{2}\theta_{p\xi}\right) \exp\left(-\frac{\ln(2)}{\alpha_0^2}\frac{(\theta_1-\theta_{p\xi})^4}{n_p'^2}\right). \tag{37}$$

Under the conditions of our experiment we had $\alpha_0 = 1.5$ mrad and $\alpha = 2.784\times 2/k_p^{(0)}d = 4.1$ mrad ($d=70$ μm). At these parameters the width of the sinc^2 function in the integrand of Eq. (37) is significantly narrower than the exponent, the width of which is equal to $2\sqrt{\alpha_0|n_p'|}\approx 29$ mrad. Owing to this, the sinc^2 function can be approximated by $\delta(\theta_{p\xi})$ to give

$$\frac{dw_\perp^{(s)}(\theta_1)}{d\theta_1} \propto \exp\left(-\frac{\ln(2)}{\alpha_0^2}\frac{\theta_1^4}{n_p'^2}\right). \tag{38}$$

The validity condition of this equation is $\alpha \ll 2\sqrt{\alpha_0|n_p'|}$. In the opposite case, at $\alpha \gg 2\sqrt{\alpha_0|n_p'|}$, the exponential function in the integrand of Eq. (37) is narrower than $\sin^2$ and can approximate by the δ function $\delta(\theta_{p\xi}-\theta_1)$. The resulting expression for the single-particle angular distribution in the ⊥ geometry takes the form

$$\frac{dw_\perp^{(s)}(\theta_1)}{d\theta_1} \propto \mathrm{sinc}^2\left(\frac{k_p^{(0)}d}{2}\theta_1\right) = \mathrm{sinc}^2\left(\frac{2.784\,\theta_1}{\alpha}\right). \tag{39}$$

This is the case when noncollinear SPDC processes give almost zero contribution to the single-particle photon angular distribution. The result of Eq. (39) can be obtained directly from Eq. (22), in which noncollinear SPDC processes are not included. Though, as said above, in a general case, Eq. (22) is valid only for calculations of the coincidence distribution. Note, however, that at given values of the slit width $d = 70$ μm and pump angular divergence in the ξ direction $\alpha = 4.1$ mrad the result of Eq. (39) is valid only at extremely small values of the angular divergence in the η direction, $\alpha_0 \ll \alpha^2/4|n_p'| \approx 2.9\times 10^{-5}$ mrad. Only for such extremely well collimated pump beams contribution of noncollinear SPDC processes into the single-particle angular distribution in the ⊥ geometry is small and can be ignored. In all other cases, when $\alpha_0 \gtrsim 2.9\times 10^{-5}$ mrad, the noncollinear SPDC processes are important and they change significantly the shape of the ⊥-geometry single-particle distribution (38) compared to that of Eq. (39) where the noncollinear SPDC processes are ignored.

Finally, if we do not use any slits and take the pump Gaussian in both directions ξ and η with the same angular width α_0, Eq. (37) is replaced by

$$\frac{dw_\perp^{(s)}(\theta_1)}{d\theta_1} \propto \int d\theta_{p\xi} \exp\left(-\frac{4\ln(2)\theta_{p\xi}^2}{\alpha_0^2}\right) \times \exp\left(-\frac{\ln(2)}{\alpha_0^2}\frac{(\theta_1-\theta_{p\xi})^4}{n_p'^2}\right). \tag{40}$$

Under the condition $\alpha_0 \ll 4|n_p'| \approx 0.57$ rad (which is always valid) the first exponential function in the integrand of Eq. (40) is much narrower than the second one, and its approximation by the δ function returns us to Eq. (38). Hence, Eq. (38) is valid for both types of experiments, with and without slit, and in both cases noncollinear SPDC processes are equally important.

E. SPDC angular distributions and the width-ratio parameters

The coincidence and single-particle photon angular distributions in the ∥ and ⊥ geometries, determined correspondingly by Eqs. (24), (32), (25), and (37), are plotted in Fig. 4. The chain-line curve in Fig. 4(a) corresponds to the approximate super-Gaussian single-particle ∥-geometry distribution of Eq. (33), whereas the dashed curve corresponds to the exact distribution of Eq. (32). Comparison of these two curves shows that the super-Gaussian curve does not describe appropriately asymmetry of the distribution but otherwise reproduces sufficiently well its structure and width. The dotted lines in both figures describe the pump angular distribution in its dependence on $\theta_{p\xi}$. It is clearly seen in Fig. 4(b) that the ⊥-geometry coincidence curve is 2 times wider than the pump, in accordance with Eq. (25).

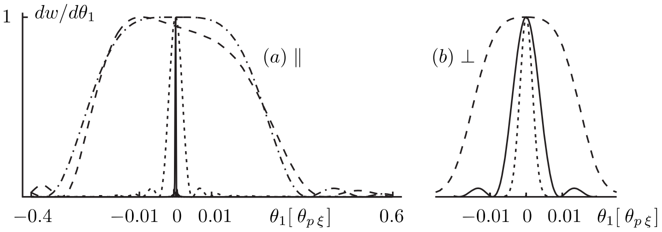

FIG. 4. Coincidence (solid lines) and single-particle (dashed lines) photon distributions in (a) $\|$ and (b) $\perp$ geometries. The chain line in (a) is the approximation of the coincidence curve in the $\|$ geometry by Eq. (33). The dotted lines show the pump (26) in its dependence on $\theta_{p\xi}$. All curves are normalized by one at their maxima.

The half-height widths of the coincidence and single-particle distributions shown in Fig. 4 are found to be equal to

$$\Delta\theta_1^{(c)\|} = 0.5 \ \text{mrad}, \quad \Delta\theta_1^{(s)\|} = 47.3 \ \text{mrad},$$

$$\Delta\theta_1^{(c)\perp} = 8.23 \ \text{mrad}, \quad \Delta\theta_1^{(s)\perp} = 29.56 \ \text{mrad}. \qquad (41)$$

Contrast between two coincidence distributions ($\|$ and $\perp$) can be characterized by the ratio of the corresponding widths $\Delta\theta_1^{(c)\perp}/\Delta\theta_1^{(c)\|} \approx 16.5$. This estimate shows that the coincidence angular distributions depend strongly on the crystal orientation. In this sense they are anisotropic and the degree of anisotropy is very high.

Analytical formulas for the coincidence and single-particle widths follow directly from Eqs. (24), (25), (33), and (38):

$$\Delta\theta_1^{(c)\|} = \frac{2.784 \times 4n_o}{Lk_p^{(0)}|n_p'|}, \quad \Delta\theta_1^{(s)\|} = 2\sqrt{|n_p'|\alpha},$$

$$\Delta\theta_1^{(c)\perp} = 2\alpha, \quad \Delta\theta_1^{(s)\perp} = 2\sqrt{|n_p'|\alpha_0}. \qquad (42)$$

The single-particle to coincidence width ratios found numerically and analytically are given by

$$R_\| = \frac{\Delta\theta_1^{(s)\|}}{\Delta\theta_1^{(c)\|}} \approx 94.6 \gg 1, \quad R_\perp = \frac{\Delta\theta_1^{(s)\perp}}{\Delta\theta_1^{(c)\perp}} \approx 3.6 \qquad (43)$$

and

$$R_\| = \frac{Lk_p^{(0)}|n_p|^{3/2}\sqrt{\alpha}}{5.568n_o}, \quad R_\perp = \frac{\sqrt{|n_p'|\alpha_0}}{\alpha}. \qquad (44)$$

For description of experiments without a slit we must replace α by α_0 in Eqs. (42) for $\Delta\theta_1^{(s)\|}$ and $\Delta\theta_1^{(c)\perp}$. This reduces values of these two widths and, numerically, makes them equal to $\Delta\theta_1^{(s)\|} \approx 28.6$ mrad and $\Delta\theta_1^{(c)\perp} \approx 3$ mrad. Also this changes both functional dependencies and numerical values of the width-ratio parameters R, which take the form

$$R_\| = \frac{Lk_p^{(0)}|n_p'|^{3/2}\sqrt{\alpha_0}}{5.568n_o} \approx 58, \quad R_\perp = \sqrt{\frac{|n_p'|}{\alpha_0}} \approx 9.8. \qquad (45)$$

So, by comparing these results with those of Eqs. (43) and (44), we see that the use of a slit emphasizes rather pronouncedly the anisotropy effect (characterized by the ratio $\Delta\theta^{(c)\perp}/\Delta\theta^{(c)\|}$) and contrast between the parameters $R_\|$ and $R_\perp$.

F. Entanglement

Thus, all three parameters $R_\|$, C_{EPR}, and C_{H} are of the same order of magnitude and are equally valid for evaluating the degree of entanglement accumulated in biphoton states under consideration. However, it should be kept in mind that these states are two dimensional, whereas the derived expressions for the parameters $R_\|$, C_{EPR}, and C_{H} reflect a contribution to entanglement only from measurements (calculations) in one (ξ) dimension [in spite of the fact that partially two dimensionality is taken into account in single-particle distributions via noncollinear phase-matching SPDC processes]. The simplest way of characterizing the overall degree of entanglement of a 2D biphoton state consists in defining such an entanglement quantifier as the product $R = R_\| R_\perp$, where $R_\perp$ reflects the contribution from the second (η) dimension. Such a definition has some reasons. Indeed, for isotropic bihoton states of the form (11), with the sinc^2 function substituted by the Gaussian function, the wave function takes the form of a product of two terms depending separately on $k_{1,2\xi}$ and on $k_{1,2\eta}$. In this case the overall Schmidt number K appears to be given by the squared 1D Schmidt number, $K = K_\xi^2 = K_\eta^2$ [10]. For anisotropic 2D double-Gaussian wave functions, similarly, the overall Schmidt number is given by the product of 1D Schmidt numbers (which can differ from each other), $K = K_\xi K_\eta$. Without the substitution sinc^2 $\to$Gaussian, the wave function (11) does not factorize. But the numerically calculated 2D Schmidt number was shown [10] to be rather close to that given by the squared 1D Schmidt number. Here we consider a significantly more complicated 2D biphoton wave function (15), for which it is hardly possible to find any adequate factorizing model. Also, this wave function is too complicated for a direct calculation of the Schmidt number. Moreover, even if we would be able to calculate in any way the 2D Schmidt number, and if it would differ noticeably from the product of 1D Schmidt numbers, it would be difficult to establish its connections with 1D experimental measurements. So, we realize that the problems of defining rigorously and measuring the entanglement quantifier in nonfactorable 2D bipartite systems exist. But, having no direct solutions of these problems (at present), we suggest to use the same definition as in factorable Gaussian systems, i.e., we suggest to define the overall entanglement quantifier as the product of the width-ratio parameters found above for the parallel and perpendicular geometries. With such a definition and with the analytical formulas (44) for $R_\|$ and $R_\perp$ we obtain

$$R = R_\| R_\perp = \frac{Lk_p^{(0)}n_p'^2}{5.568n_o}\sqrt{\frac{\alpha_0}{\alpha}}. \qquad (46)$$

Numerically, at $\alpha = \alpha_0$ (no slit), $R \approx 571$. This is a really huge degree of entanglement. It arises owing to the combination of three factors: a long crystal (large L), relatively high anisotropy determined by $|n_p'|$, and not too small value of the pump angular divergence α.

G. Dependence on the pump angular divergence

To evaluate the status of the derived results in a general picture of SPDC in long anisotropic crystals, let us investigate and discuss dependencies of all the parameters we consider here on the varying angular divergence of the pump α_0. Let us assume that all other parameters of the pump and of the crystal are kept constant and are the same as used above. For simplicity let us consider here only the case of transversely isotropic pump not modified by any slits and given by Gaussian functions in both ξ and η directions with equal angular widths α_0. At varying α_0 the widths of the coincidence and single-particle photon angular distributions can be found from the same equations (23), (28), and (40), which were used above for finding these widths at a given value of α_0 (1.5 mrad) [with E_p in Eq. (23) and the first sinc^2 function in Eq. (28) substituted by the Gaussian function, as in Eq. (40)]. Such a generalization not only gives new analytical expressions for the widths, more general than those of Eqs. (42), but also determines the applicability conditions of the above-derived results. So, the coincidence distribution widths are easily found as the widths of the narrower of the two functions on the right-hand side of Eq. (23),

$$\Delta\theta_1^{(c)\parallel} = \min\{2\alpha_0, 2\alpha_{\rm cr}^{\parallel}\} \approx 2\frac{\alpha_0\alpha_{\rm cr}^{\parallel}}{\sqrt{\alpha_0^2 + \alpha_{\rm cr}^{\parallel 2}}} \qquad (47)$$

and

$$\Delta\theta_1^{(c)\perp} = \min\{2\alpha_0, 2\alpha_{\rm cr}^{\perp}\} \approx 2\frac{\alpha_0\alpha_{\rm cr}^{\perp}}{\sqrt{\alpha_0^2 + \alpha_{\rm cr}^{\perp 2}}}, \qquad (48)$$

where

$$\alpha_{\rm cr}^{\parallel} = \frac{2\times 2.784 n_0}{Lk_p^{(0)}|n_p'|},$$

$$\alpha_{\rm cr}^{\perp} = 2\sqrt{\frac{2\times 2.784 n_0}{Lk_p^{(0)}}} = 2\sqrt{\alpha_{\rm cr}^{\parallel}|n_p'|}. \qquad (49)$$

Numerically $\alpha_{\rm cr}^{\parallel} \approx 0.25$ mrad and $\alpha_{\rm cr}^{\perp} \approx 12$ mrad. These two constants determine the points $\alpha_0 = \alpha_{\rm cr}^{\parallel,\perp}$ in vicinities of which dependencies of widths on α_0 change their character. Note that the arising, in Eqs. (47) and (48), minimum and (below) maximum functions describe dependencies, which are not smooth. In reality the angular distribution widths depend on α_0 smoothly, and the root-square expressions in Eqs. (47) and (48) give rather good representation of these smooth dependencies.

Similarly, the widths of the single-particle distributions, found from Eqs. (28) and (40) appear to be equal for both $\parallel$ and $\perp$ geometries and given by

$$\Delta\theta_1^{(s)\parallel} = \Delta\theta_1^{(s)\perp} = \max\{2\sqrt{\alpha_{\rm cr}^{\parallel}|n_p'|}, \sqrt{2\alpha_0|n_p'|}\} \approx 2\sqrt{|n_p'|}\sqrt{\alpha_0 + \alpha_{\rm cr}^{\parallel}}. \qquad (50)$$

Altogether the dependencies of wave-packet widths on α_0 are shown in Fig. 5 in a double-logarithmic scale.

In addition to $\alpha_{\rm cr}^{\parallel,\perp}$, the intermediate grid line shown in Fig. 5 indicates the value of $\alpha_0 = 1.5$ mrad that has occurred in our experiment.

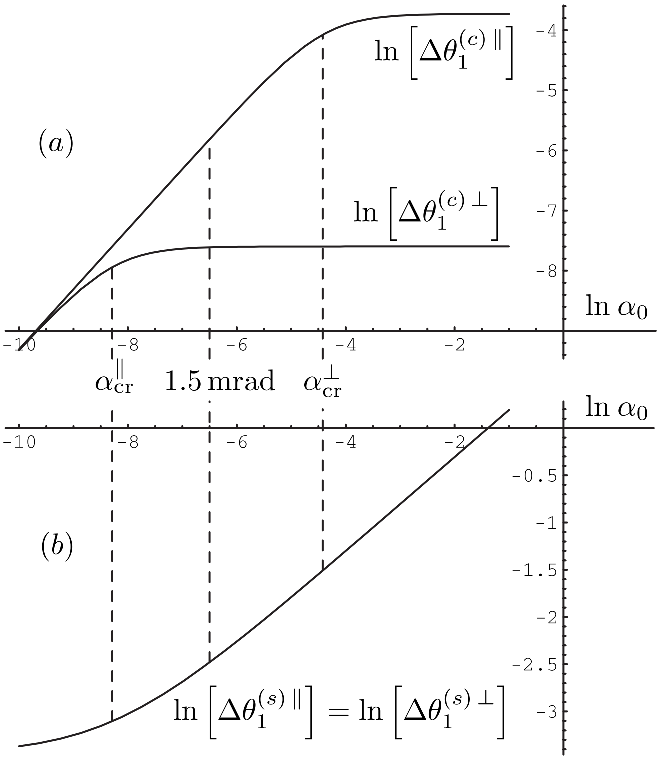

FIG. 5. (a) Coincidence and (b) single-particle widths vs the pump angular divergence α_0.

The width-ratio parameters are easily found with the help of Eqs. (47), (48), and (50),

$$R_{\parallel}(\alpha_0) = \frac{\sqrt{|n_p'|(\alpha_0 + \alpha_{\rm cr}^{\parallel})}\sqrt{\alpha_0^2 + \alpha_{\rm cr}^{\parallel 2}}}{\alpha_0\alpha_{\rm cr}^{\parallel}} \qquad (51)$$

and

$$R_{\perp}(\alpha_0) = \frac{\sqrt{|n_p'|(\alpha_0 + \alpha_{\rm cr}^{\parallel})}\sqrt{\alpha_0^2 + \alpha_{\rm cr}^{\perp 2}}}{\alpha_0\alpha_{\rm cr}^{\perp}}. \qquad (52)$$

The curves describing the functions $R_{\parallel}(\alpha_0)$ and $R_{\perp}(\alpha_0)$, as well as their product $R_{\rm overall}(\alpha_0) = R_{\parallel}(\alpha_0)R_{\perp}(\alpha_0)$, are shown in Fig. 6, in the same double-logarithmic scale as in Fig. 5. The curve $R_{\rm overall}(\alpha_0)$ is seen to have a rather long plateau in the region

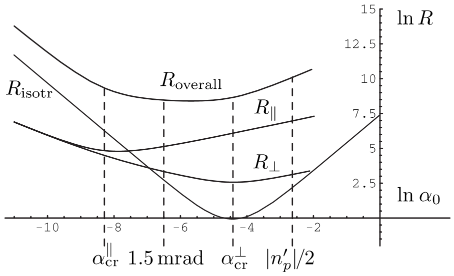

FIG. 6. The width-ratio parameters $R_{\parallel}$, $R_{\perp}$, and $R_{\rm overall}$ vs the pump divergence α_0; the same overall width-ratio parameter for isotropic wave function.

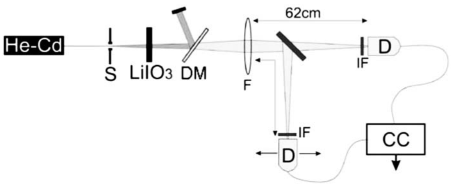

FIG. 7. Experimental setup for measuring single and coincidence probability distributions.

$$\alpha_{\mathrm{cr}}^{\parallel} \leqslant \alpha_0 \leqslant \alpha_{\mathrm{cr}}^{\perp}. \tag{53}$$

These inequalities determine the applicability conditions of all the results derived above. The grid line at $|n_p'|/2$ indicates the limit above which some of the approximations used above fail [e.g., the approximation $\theta_1 \leqslant |n_p'|$ used in simplifications of Eqs. (29) and (35)].

The fourth curve with a deep minimum shown in Fig. 6 is the same overall width-ratio parameter but calculated for isotropic wave function, i.e., for a model system with all the same parameters as in LiIO$_3$ but with $n_p'=0$. This system is considered just for a comparison and for showing an importance of anisotropy. For isotropic wave function both coincidence and single-particle widths are independent of a geometry. The coincidence widths coincide with those found above for the $\perp$ geometry [Eq. (48)]. As for the single-particle width, it can be easily found, e.g., from Eq. (28) with $n_p'=0$ to be given by

$$\Delta\theta_{\mathrm{isotr}}^{(s)} = \max\{\alpha_0, \ \alpha_{\mathrm{cr}}^{\perp}\} \approx \sqrt{\alpha_0^2 + \alpha_{\mathrm{cr}}^{\perp 2}}. \tag{54}$$

The resulting overall width-ratio parameter can be presented in a standard form [10,13]

$$R_{\mathrm{isotr}} = \frac{1}{4}\left(\eta + \frac{1}{\eta}\right)^2, \tag{55}$$

where the control parameter η is given by

$$\eta = \frac{\alpha_0}{\alpha_{\mathrm{cr}}^{\perp}}. \tag{56}$$

The curves of Fig. 6 show that the width-ratio parameter found for the isotropic system is significantly smaller than for the anisotropic one.

The shape of the curve $R_{\mathrm{overall}}(\alpha_0)$ in Fig. 6 shows that entanglement of biphoton states can be further increased by taking either extremely narrow ($\alpha_0 < \alpha_{\mathrm{cr}}^{\parallel}$) or extremely wide ($\alpha_0 > \alpha_{\mathrm{cr}}^{\perp}$) pump laser beams, i.e., outside of the region of parameters (53) we consider here.

IV. EXPERIMENT

A. Experimental setup

The experimental setup is shown in Fig. 7. To generate the entangled photons we use type I and 15-mm-length lithium-iodate crystal pumped with a 5-mW cw-helium-cadmium laser operating at 325 nm. The correlated photons generated via SPDC process with equal polarization and wavelength 650 nm are separated from the pump by dichroic mirror. Interference filters centered at 650 nm with a bandwidth of 10 nm are placed in each arm of Brown-Twiss scheme. To measure coincidence and single-photon distributions in the transverse momenta we use the lens with focal length $F=62$ cm. Two single-photon detectors are positioned in focal plane of the lens. Such detector arrangement allows one to measure the momentum distribution(s) by scanning one or both detectors along the certain direction. In most of the cases we fix position of the first detector at the maximum of count rate and scan another one to register both distributions as a function of detector displacement. Since detector moves in the focal plane its position (x) relates to the angular mismatch (θ) as $x=F\tan\theta$.

TABLE I. Angular anisotropy parameter n_p' for different nonlinear crystals.

Crystal	Phase-matching angle φ_0 (deg)	n_p'
LBO	51.47	−0.0270
KDP	54.33	−0.0395
BBO	36.44	−0.1175
LiIO$_3$	60.44	−0.1436

B. Results and discussion

The main idea behind the performed experiment is to check the formulas (42)–(44) and compare the $\parallel$ and $\perp$ geometries (see Fig. 1). One of the key parameters of the theory described above is the pump angular width. Originally our He-Cd laser had the angular width equal to 1.5 mrad. To see in experiment how the angular distribution of the pump affects biphoton angular distributions, we have artificially anisotropically broadened the pump distribution in angles by installing a slit in front of the crystal. As a result, the pump angular distribution remains localized along the direction parallel to the slit (at the same level of 1.5 mrad as was without a slit) but it spreads in the orthogonal direction. The slit thickness was 70 μm wide, which corresponds to the 4.1 mrad pump angular width in the direction perpendicular to the slit. Alternatively we have used in some measurements a lens instead of a slit to provide axially symmetric (isotropic) broadening of the pump up to the width of 15 mrad. Comparison of results of such measurements was used for evaluating the role of the pump angular broadening for efficiency of emission processes arising under the noncollinear phase-matching conditions.

Another key parameter is angular derivative of the pump extraordinary refractive index n_p' near the exact phase-matching direction Oz'. Table I shows this value for different crystals available for producing photon pairs. It shows that lithium iodate is the best candidate because in this crystal the derivative $|n_p'|$ takes a rather large value. Besides, the effect of high entanglement anisotropy discussed in the paper depends strongly on the product Ln_p'. So, the second reason why we chose this crystal is that the sample of lithium iodate can be made rather long.

As it follows from theory developed above, at sufficiently high values of $|n_p'|$ the coincidence angular distribution of

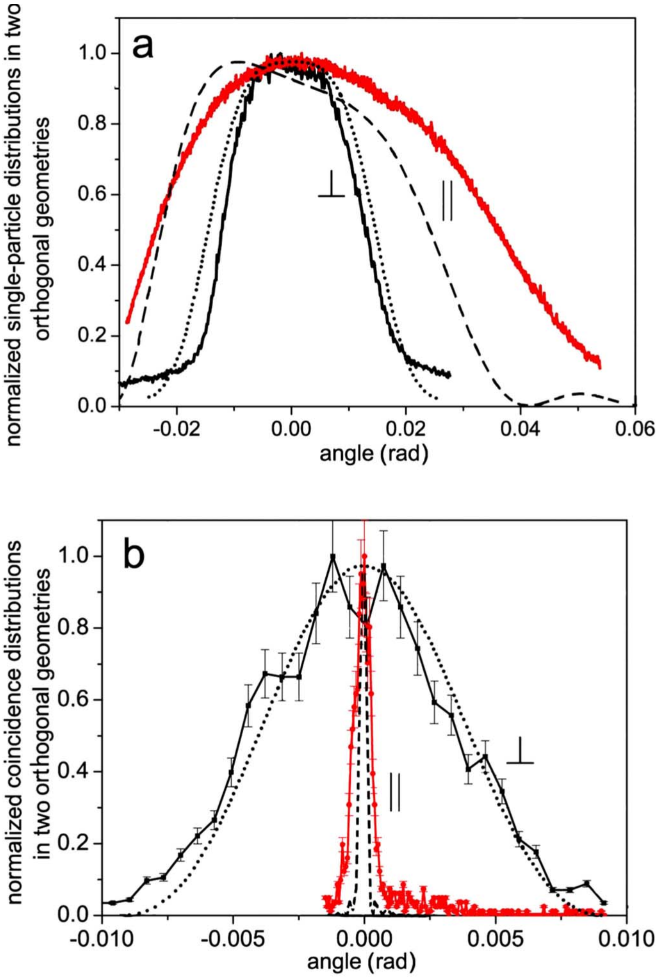

FIG. 8. (Color online) Angular distributions of (a) single and (b) coincidences counts for two orthogonal geometries (⊥) and (∥).

biphotons in the ∥ geometry does not depend at all on the divergence of the pump [see Eq. (25)]. Moreover, being determined completely by properties of the crystal and, in particular, by anisotropy of the refractive index, the width of the coincidence distribution can be done even narrower than the pump angular width. At the same time the width of the single-photon distributions grows up with the pump broadening. Both narrowing of the coincidence and broadening of the single-particle angular distributions are factors resulting in a growing degree of entanglement.

As mentioned above, in the experiment the detection plane was always horizontal. The slit was installed vertically to provide angular broadening in the horizontal direction, whereas the crystal optical axis could be lying in arbitrary plane. We considered the following two situations: (a) Detection and pump angular broadening directions are along the $O'x'$ axis, i.e., in the ∥ plane or in the plane containing laser and optical axes and (b) both detection and pump angular broadening directions are along the $O'y'$ axis, i.e., in the ⊥ plane, and these directions are perpendicular to the plane containing laser and optical axes.

Figure 8 shows two sets of experimental angular distributions (solid line) received in (a) single-particle and (b) coincidences measurements, which are plotted together for different geometries, with a slit broadened pump beam. These pictures illustrate clearly that in the ∥ geometry coincidence distribution becomes narrower whereas the single-particle distribution broadens in comparison with the ⊥ geometry. The corresponding ratios are $\Delta k_{\perp}^{(c)}/\Delta k_{\parallel}^{(c)}=11$ for coincidences and $\Delta k_{\perp}^{(s)}/\Delta k_{\parallel}^{(s)}=0.42$ for singles.

For comparison, the corresponding theoretical curves are also shown in Fig. 8 (dotted and dashed lines). Qualitatively, the corresponding experimental and theoretical curves are seen to be very similar. Quantitatively, the theoretical estimates of the coincidence widths are $\Delta k_{\perp}^{(c)}/\Delta k_{\parallel}^{(c)}=16$ and $\Delta k_{\perp}^{(s)}/\Delta k_{\parallel}^{(s)}=0.60$. The difference between theoretical and experimental results is not too high, though quite visible. Probably, it has different origin for coincidence and single width ratios.

In the case of coincidence counts, we think that the main reason for a difference between the theoretical and experimental width ratios is related to some external factors owing to which the experimentally measured coincidence width is larger than the theoretical estimate (0.75 mrad in experiment compared to 0.5 mrad in theory). As for the single-particle width, probably in experiment the corresponding curve in the ⊥ geometry did experience some broadening arising from the noncollinear phase-matching emission processes, in spite of the missing slit broadening of the pump angular distribution in the $O'x'$ direction.

Figures 9(a) and 9(b) present the same experimental results only differently regrouped, which allows one to evaluate the experimentally found degree of entanglement.

Figure 9(a) corresponds to the case when detector is scanning in the plane perpendicular to the optical axis (⊥ geometry), and the slit broadens the pump angular distribution in the same direction. The width of the single-particle distribution is 25 mrad whereas the width of the coincidence one is 8.4 mrad, i.e., 2 times wider than the width of the pump [in accordance with Eq. (25)]. The ratio $\frac{\Delta k_{1\perp}^{(s)}}{\Delta k^{c}(s)_{1\perp}}=3$, so the degree of entanglement is not very high. Note, that in the above-presented theory we have obtained, for this ratio, even a little bit higher value, 3.6.

The results occurring in the case when both scanning and pump broadening occur in the plane containing the crystal optical axis (∥ geometry) are shown in Fig. 9(b). Here the widths of single and coincidence distributions are 60 mrad and 0.75 mrad correspondingly. Their ratio is 80, which is much greater than in the previous case though it is somewhat less than the corresponding theoretical estimate $R_{k\parallel}=94.6$ in (43). At the same time one should remember that the biphoton state is two dimensional. The measure R_{overall} introduced above takes the value 240. Although it is distinctly less than the value estimated numerically in (46) we think that the difference can be attributed only to some external factors affecting experiment. In the case of the ∥ geometry the above-discussed noncollinear phase-matching processes are completely taken into account in the theoretical derivation, and the explanation of the theory-experiment discrepancies given above for the ⊥ geometry does not work for the ∥ geometry.

The width of the photon coincidence angular distribution is shown in Fig. 10 in its dependence on the angle χ deter-

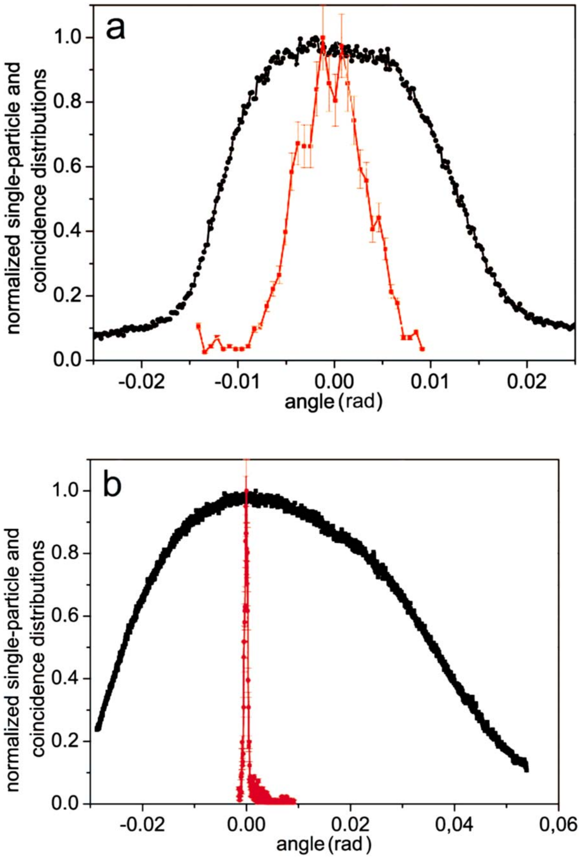

FIG. 9. (Color online) Experimental results: Normalized single-particle and coincidence distributions for (a) ⊥ geometry and (b) ∥ geometry. Curves with errors are the coincidence. The pump is broadened by a slit.

mining orientation of the crystal and defined in Fig. 2, $\chi=0$ and $\chi=90$ correspond to the horizontal and vertical geometries. Theoretical and experimentally measured curves are shown in the dashed and solid lines. In polar coordinates the angular coincidence distribution looks like an ellipse, with its major axis oriented along the vertical direction.

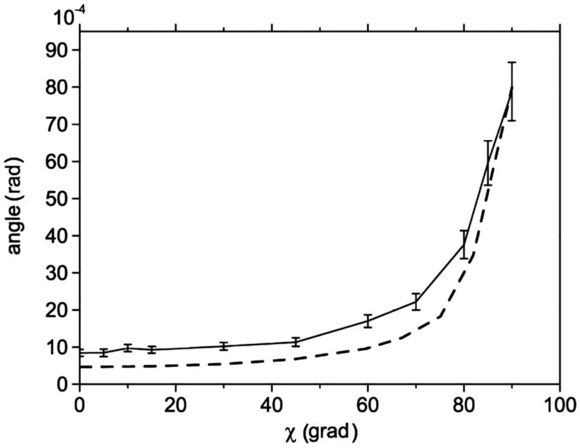

FIG. 10. Dependence of the coincidence distributions widths on tilting angle χ, theory and experiment (correspondingly, the dashed and solid lines).

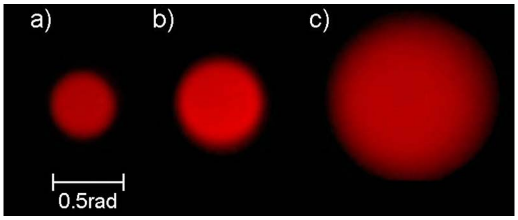

FIG. 11. (Color online) Photographs of angular SPDC spectrum at different pump broadening. (a) Originally pump angular width (1.5 mrad), (b) anisotropically broadened pump in horizontal plane, (c) anisotropically broadened pump in vertical plane (slit with thickness 70 μm). The optical axis of the crystal was installed horizontally.

Comparison of the theoretical and experimental curves in Fig. 10 shows that they are rather close, though a small difference between them exceeds the error bars. As mentioned above, an origin of this small difference is not quite clear and we think that it can be related to some external factors occurring in experiments and not taken into account in the theory.

Let us return to the consideration of single-particle angular distributions. The theory and experiment have shown the difference between the widths measured in two orthogonal geometry. However in 2D spectrums its anisotropic features do not manifest themselves clearly as in coincidences. Figure 11 presents the photograph pictures of the 2D SPDC spectrum. An interference filter centered at 650 nm with bandwidth of 10 nm was placed after the crystal for frequency selection. The single-particle distributions in the far-field zone were registered by a digital photographic camera Nikon D70. Each frame was made with the exposure time 30 s. Figure 11(a) shows the angle distribution of SPDC which was made without any slit before the crystal. Figures 11(b) and 11(c) correspond to the anisotropic broadening of the pump: In the first case the slit was oriented collinear to the optical axis (⊥ geometry), in another one the slit was orthogonal to the optical axis (∥ geometry). These photos illustrate clearly that 2D angle distributions have different radii in orthogonal geometries, but the section of each of them is a circle.

In some experimental measurements we have used a lens instead of a slit. A lens has provided equal angular broadening of the pump up to the width of 15 mrad, so it is impossible to distinguish its contribution to spreading in ∥ or ⊥ planes.

Figure 12 presents single-particle and coincidence distributions for two orthogonal geometries, ⊥ and ∥. In this case the width of single-particle distribution, measured in ⊥ plane is the same as in the ∥ plane.

However, another observed effect which connected with the narrowing of the coincidence distribution is reserved. The width of the coincidence distribution in the ∥ geometry stays narrower than the pump angular width whereas in the ⊥ geometry the width of the coincidence distribution becomes wider. Note also that in the case of lens broadening the values of the entanglement parameter R_k appear to be somewhat smaller than in the case of slit broadening in both ⊥ and ∥ geometries: in the case of lens broadening $R_{k\perp}$

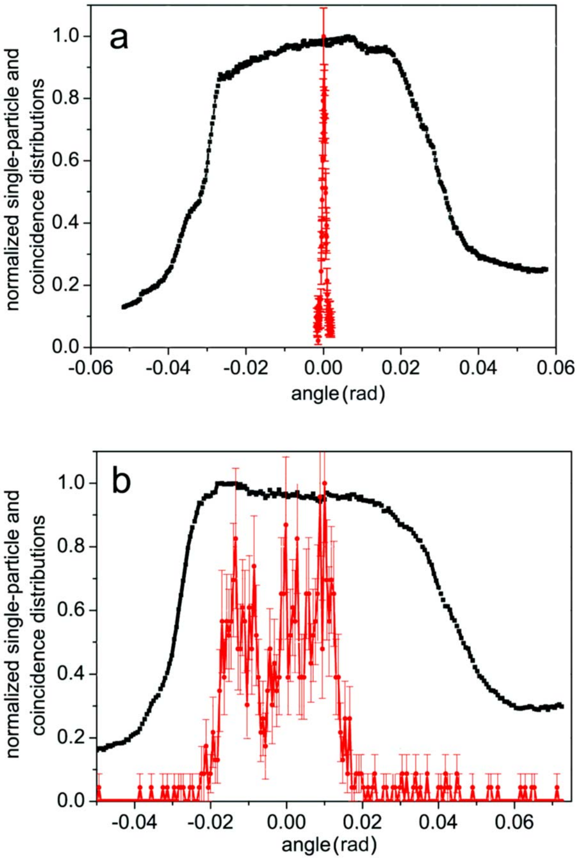

FIG. 12. (Color online) Experimental results: Normalized single-particle and coincidence distributions for (a) ∥ and (b) ⊥ geometries. Curves with errors are the coincidence. The pump is broadened by a lens.

$=2.6$ and $R_{k\|}=75$. But the main qualitative conclusions remain the same as earlier: At chosen values of the parameters almost no entanglement can be seen in the ⊥ geometry and a very high entanglement can be and was observed in the ∥ geometry.

V. CONCLUSION

In conclusion, we have shown both theoretically and experimentally that there are two different schemes of observing SPDC biphoton wave packets. In the traditional and alternative schemes the detector scanning is assumed to be performed in the planes, correspondingly, perpendicular and parallel to the plane containing optical and laser axes. Owing to the anisotropy of the crystal refractive index for the extraordinary wave, a structure of the coincidence and single-particle biphoton wave packets observable in these two schemes are significantly different. In the alternative scheme, coincidence wave packets demonstrate a very strong narrowing compared to the traditional scheme, whereas the single-particle wave packets broaden. All of this results in a very high degree of entanglement that can be observed in the alternative scheme of observations, and cannot be seen in the traditional scheme. The overall entanglement parameter determined as a product of the ratios of the single to coincidence wave-packet widths in two geometries appears to be as high as about 240 according to experimental measurements and even 2 times larger in theoretical estimates. The degree of the coincidence wave-packet narrowing is shown to be so strong that in the alternative scheme of observations the coincidence wave packet appears to be much narrower than the angular distribution of the pump.

In this work we have restricted our analysis by the photon angular distributions only. But, clearly, the anisotropy effects should be seen also in the coordinate coincidence and single-particle biphoton distributions in the near zone. In the noncollinear regime of parametric scattering this was demonstrated in Ref. [17]. For the collinear regime investigation of the anisotropy effects in the coordinate representation will be reported elsewhere. Here we would like to stress that there is a serious difference in physics of anisotropic effects in the coordinate and angular picture. In the coordinate picture the reason why the biphoton distributions can be anisotropic is related to the spatial walk-off effect. In the angular distribution the anisotropic structure of the extraordinary wave refractive index manifests itself as a kind of an angular filter for the pump. Even if the pump angular divergence is relatively large, in the geometry with crystal optical axis lying in the observation plane the angle-dependent refractive index of the extraordinary wave effectively filters off components of the pump propagating at large angles with respect to the laser axis. Such filtering makes a rather poorly collimated pump behaving as an extremely narrow light beam with a very small angular divergence, which gives rise to a very narrow coincidence angular biphoton distribution and to a very high degree of entanglement.

ACKNOWLEDGMENTS

This work was supported in part by the Russian Foundation for Basic Research (Contracts Nos. 05-02-16469 and 06-02-16769), the Dynasty Foundation, the Russian Federation President's Grant No. MK1283.2005.2, the Leading Russian Scientific Schools (Grant No. 4586.2006.2), and by the U.S. Army International Technology Center, Atlantic, Grant No. RUE1-1616-MO-06.

---

[1] A. Einstein, B. Podolsky, and N. Rosen, Phys. Rev. **47**, 777 (1935).
[2] E. Schrödinger, in *Quantum Theory and Measurement*, edited by J. A. Wheeler and W. H. Zurek (Princeton University Press, New York, 1983).
[3] M. H. Rubin, Phys. Rev. A **54**, 5349 (1996).
[4] A. V. Burlakov, M. V. Chekhova, D. N. Klyshko, S. P. Kulik, A. N. Penin, Y. H. Shih, and D. V. Strekalov, Phys. Rev. A **56**,

3214 (1997).

[5] C. H. Monken, P. H. Souto Ribeiro, and S. Padua, Phys. Rev. A **57**, 3123 (1998).

[6] S. P. Walborn, A. N. de Oliveira, S. Padua, and C. H. Monken, Phys. Rev. Lett. **90**, 143601 (2003).

[7] M. D'Angelo, Y.-H. Kim, S. P. Kulik, and Y. Shih, Phys. Rev. Lett. **92**, 233601 (2004).

[8] C. Kurtsiefer, M. Oberparleiter, and H. Weinfurter, Phys. Rev. A **64**, 023802 (2001).

[9] R. S. Bennink, Y. Liu, D. D. Earl, and W. P. Grice, Phys. Rev. A **74**, 023802 (2006).

[10] C. K. Law and J. H. Eberly, Phys. Rev. Lett. **92**, 127903 (2004).

[11] K. W. Chan, C. K. Law, and J. H. Eberly, Phys. Rev. A **68**, 022110 (2003).

[12] J. C. Howell, R. S. Bennink, S. J. Bentley, and R. W. Boyd, Phys. Rev. Lett. **92**, 210403 (2004).

[13] M. V. Fedorov, M. A. Efremov, P. A. Volkov, and J. H. Eberly, J. Phys. B **39**, S467 (2006).

[14] M. V. Fedorov, M. A. Efremov, A. E. Kazakov, K. W. Chan, C. K. Law, and J. H. Eberly, Phys. Rev. A **69**, 052117 (2004).

[15] M. V. Fedorov, M. A. Efremov, A. E. Kazakov, K. W. Chan, C. K. Law, and J. H. Eberly, Phys. Rev. A **72**, 032110 (2005).

[16] M. V. Fedorov, M. A. Efremov, and P. A. Volkov, Opt. Commun. **264**, 413 (2006).

[17] J. P. Torres, G. Molina-Terriza, and L. Torner, J. Opt. B: Quantum Semiclassical Opt. **7**, 235 (2005); C. I. Osorio, G. Molina-Terriza, B. G. Font, and J. P. Torres, Opt. Express **15**, 14636 (2007).

[18] R. Grobe, K. Rzazewski, and J. H. Eberly, J. Phys. B **27**, L503 (1994).

[19] A. Ekert and P. L. Knight, Am. J. Phys. **63**, 415 (1995).